Nanoscale

PAPER

Purely substitutional nitrogen on graphene/Pt(111) unveiled by STM and first principles calculations

Ana Martín-Recio,[a] Carlos Romero-Muñiz,[b] Pablo Pou,[b,c] Rubén Pérez[b,c] and José M. Gómez-Rodríguez*[a,c,d]

Cite this: *Nanoscale*, 2016, **8**, 17686

Received 21st June 2016,
Accepted 26th September 2016

DOI: 10.1039/c6nr04978h

www.rsc.org/nanoscale

Nitrogen doping of graphene can be an efficient way of tuning its pristine electronic properties. Several techniques have been used to introduce nitrogen atoms on graphene layers. The main problem in most of them is the formation of a variety of C–N species that produce different electronic and structural changes on the 2D layer. Here we report on a method to obtain purely substitutional nitrogen on graphene on Pt(111) surfaces. A detailed experimental study performed *in situ*, under ultra-high vacuum conditions with scanning tunneling microscopy (STM), low energy electron diffraction (LEED) and Auger electron spectroscopy (AES) of the different steps on the preparation of the sample, has allowed us to gain insight into the optimal parameters for this growth method, that combines ion bombardment and annealing. This experimental work is complemented by first-principles calculations and STM simulations that provide the variation of the projected density of states due to both the metallic substrate and the nitrogen atoms. These calculations enlighten the experimental findings and prove that the species found are graphitic nitrogen. This easy and effective technique leads to the possibility of playing with the amount of dopants and the metallic substrate to obtain the desired doping of the graphene layer.

Introduction

The atomic arrangement in the one atom thick graphene (G) layer is responsible for all the striking structural and electronic properties of this material.[1–4] Its sp^2 hybridization leads to a planar atomic array with an electronic structure close to the Fermi level dominated by the π bands generated by the remaining p orbitals, having a 0 eV band gap with linear dispersion in the vicinity of the *K*-points. As a consequence, at low energies, both electrons and holes can be described as massless Dirac fermions with a Fermi velocity only ~300 times smaller than the speed of light. This ultrahigh carrier velocity and many other electronic remarkable graphene properties make this material a certain silicon substitute in the near future.[5–8] However, in order to use graphene in electronic devices, we must first be capable of tuning its electronic structure to open the desired gap or to modify the charge carrier concentration to our whim. With this objective of tailoring graphene's electronic properties, acceptor/donor centers, such as boron or nitrogen atoms, have been already intensively studied.[9–14] Also, the nitrogen-doped graphene, in which we will focus in this work, has proved to have unique catalytic properties in several electrochemical reactions,[15–19] such as oxygen or hydrogen peroxide reduction for fuel cell applications and biosensors.[16–19] For all these reasons, N-doped graphene has already been grown following several different methods such as chemical vapor deposition (CVD),[20–25] nitrogen plasma treatment,[9,26–29] redox reactions,[8] ion implantation[13,30,31] or an improved version of this last one.[12,32,33] This modified technique, basically consisting on annealing the sample to high temperatures after the ion bombardment, has already proved to result in better samples with only two kind of nitrogen species on graphene on metals: graphitic and pyridinic nitrogen (see Fig. 1).[12] It has been determined that the substitutional or graphitic nitrogen structure is energetically more favorable although pyridinic nitrogen can also be kinetically stable when surface defects do exist or have been created during bombardment.[23,32,34,35] For this reason, graphene grown on metals could be a good platform for these studies due to the high quality and crystallinity of pristine graphene on these substrates.[36–38] Besides, the shift of graphene's Dirac cone on the graphitic and pyridinic centers are opposite: substitutional nitrogen will n-dope the sample while pyridinic nitrogen shifts the π band on the opposite direction.[22,23] Thus, in a sample with both kind of species, one will cancel the doping effect of the other.

[a]*Departamento de Física de la Materia Condensada, Universidad Autónoma de Madrid, E-28049 Madrid, Spain. E-mail: josem.gomez@uam.es*
[b]*Departamento de Física Teórica de la Materia Condensada, Universidad Autónoma de Madrid, E-28049 Madrid, Spain*
[c]*Condensed Matter Physics Center (IFIMAC), Universidad Autónoma de Madrid, E-28049 Madrid, Spain*
[d]*Instituto Nicolás Cabrera, Universidad Autónoma de Madrid, E-28049 Madrid, Spain*

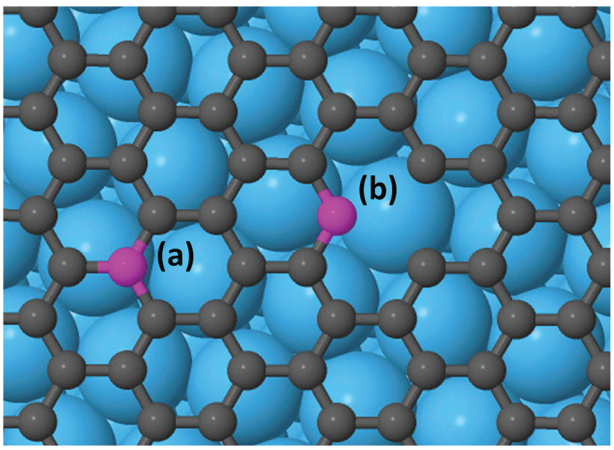

Fig. 1 G/Pt(111) scheme (Pt atoms in blue and C atoms in gray) with two nitrogen atoms (pink) incorporated to the graphene lattice in two different ways: (a) graphitic or substitutional nitrogen in which a nitrogen atom has replaced a carbon atom. (b) Pyridinic nitrogen in which the nitrogen has replaced a carbon atom with only two bonds with its neighbouring C atoms. Pyridinic nitrogen is always related with defects in the 2D layer.

Creating purely graphitic nitrogen on graphene on metals seems then to be an interesting issue to tackle and that has not been reached yet. For this reason, we report here a thorough study on the nitrogen ion implantation + annealing method that, on a highly crystalline graphene/Pt(111), results on a purely graphitic nitrogen–graphene sample. An advantage of using Pt(111) as the substrate is that its very low graphene–metal coupling leads to the formation of almost flat graphene moiré patterns[39] that will allow us to distinguish and analyze the nitrogen structure on the 2D atomic lattice. We suggest that the annealing procedure facilitates atom recombination and elimination of the defects created during bombardment, leading to only substitutional nitrogen on the sample. Some hints of this behavior will be shown on our scanning tunneling microscopy (STM) images measured before and after annealing the sample. Also, the ion energy range for a good sample growth is shown through the combination of STM with low energy electron diffraction (LEED) and Auger electron spectroscopy (AES) techniques. Lastly, with density functional theory (DFT) calculations, graphene's structural and electronic behavior near the nitrogen centers will be shown and discussed. With the aid of STM simulations based on these DFT results, the structures resolved on the experimental measurements are finally unveiled and unequivocally related to the graphitic configuration of nitrogen on graphene grown on Pt(111) substrate.

Methods

Experimental details

Experiments and sample preparation were carried out under ultra-high vacuum conditions (UHV) with a base pressure below 1×10^{-10} Torr. The system is equipped with a variable temperature scanning tunneling microscope (VT-STM)[40,41] that operates in a temperature range from 40 K to 400 K and with a four-grid LEED/AUGER system for the characterization of the surfaces.

The Pt(111) surface was cleaned by cycles of argon bombardment at 1 kV and annealing at 800 °C while keeping the sample in an oxygen atmosphere ($P_{oxygen} = 5 \times 10^{-7}$ Torr) to avoid carbide formation at the surface from carbon segregation from the bulk. The graphene monolayer was grown *via* chemical vapor deposition (CVD) of low pressure (3×10^{-7} Torr) ethylene (C_2H_4) at 1000 °C. Such a procedure results in large, defect-free graphene areas.[42] After the graphene surface was checked with LEED, we proceeded with the nitrogen irradiation performed by means of a simple ion gun (the same that was used for cleaning purposes) in which nitrogen molecules were ionized by electron impact and then accelerated against the sample with a certain energy and an angle of 45° with respect to normal incidence. Finally, the bombarded sample was annealed to high temperatures (1000 °C) to mainly reconstruct the graphene layer. The exact parameters used for this procedure are discussed in the following sections. After that, the sample was transferred to the VT-STM chamber where the STM measurements were done at room temperature (RT). Data acquisition and image processing were performed with the WSxM software from Nanotec Electrónica S.L.[43] (http://www.wsxmsolutions.com). All AES experiments were always performed after STM measurements.

Computational details

In this work we have performed several DFT calculations using the plane wave code VASP.[44] We have used a 400 eV energy cutoff and projected augmented wave pseudopotentials.[45,46] We have employed a PBE exchange–correlation functional[47] corrected by Grimme's D2 semiemperical approach[48] to take into account dispersion forces. The parameters of the Pt for the vdW interaction, not provided by the original Grimme's DFT-D2 implementation, were C_6(Pt) = 20.00 J nm^6 mol^{-1} and R_0(vdW) = 1.900 Å which have been proved to correctly describe the G–Pt interaction.[39,49] In our simulations we have used a unit cell which reproduces the most common G/Pt(111) moiré pattern consisting in a $(3 \times 3)_G$ cell on a $[(\sqrt{7} \times \sqrt{7}) - R19°]_{Pt}$.[38,39,50] However, we have used a larger cell constituted by four moiré unit cells –a 6 × 6 supercell– with the aim of reducing the dopant concentration to more realistic values (in this case ≈1.4% atomic N/C). This unit cell is made by the superposition of a graphene mono-layer and a four-layer platinum slab with a total of 112 Pt atoms and 72 C atoms. In this case, we will remove one C atom which will be substituted by one N atom in different parts of the moiré. The experimental misfit between both lattices is very small (strain ≈0.5%) so we fixed the C–C distance of graphene at 1.42 Å and adjust the platinum lattice. The full structures were subjected to electronic self-consistent loops with an accuracy of 10^{-6} eV and further ionic relaxation following a conjugated gradient algorithm until forces upon atoms were smaller than 0.01 eV Å^{-1}. During ionic relaxations the two bottom layers are

fixed in their bulk positions while all other atoms are allowed to relax. Workfunctions have been calculated using unit cells with larger vertical spacings (more than 25 Å in z axis) to avoid interactions between periodical images and also dipole corrections have been used in the normal axis. The value was calculated as the difference between the vacuum potential (far enough from the surface, where it becomes flat) and the calculated Fermi energy. The two-dimensional Brillouin zone was sampled using a different amount of k-points depending on the calculation type. We used a 3 × 3 × 1 Monkhorst–Pack grid during ionic relaxation to find equilibrium geometries, a 5 × 5 × 1 grid when calculating workfunctions, a 11 × 11 × 1 grid for STM images and a 21 × 21 × 1 grid when calculating densities of states (25 × 25 × 1 for the free standing graphene without the metallic substrate). Finally, STM theoretical images were obtained using the Tersoff–Hamann approximation[51] from the DFT results.

Results and discussion

Modified ion implantation method on graphene on metals

As described in the experimental details, the preparation method used in this work consists of bombarding the sample with nitrogen ions and annealing it to high temperatures afterwards. In these section, we offer a detailed insight into the sample structures in each step of this preparation method by means of STM measurements.

After graphene growth, the platinum surface is covered by graphene patches with different rotational domains. In Fig. 2a, the STM image shows two of these domains in which the different orientations with respect to the metallic lattice give rise to different superstructures or moiré patterns.[39,50,52] The inset in this figure is a detailed atomically resolved STM image of one of these moiré patterns. The second step, shown in Fig. 2b, consists mainly in N_2^+ bombardment of the sample.[53–55] In this case, the energy used to accelerate the ions was 100 eV and its exposure was kept for around 10 min. As it can be seen from both STM images (Fig. 2b and its inset), the surface contains several defects of different unspecified nature. Conversely, if the sample is annealed afterwards to a temperature of 1000 °C for ~10 minutes, the surface shows only one kind of defect randomly distributed on the surface (Fig. 2c and its inset). If these defects are atomically resolved, as shown in the inset of Fig. 2c, the detailed atomic structure is disclosed: one darker atom position is surrounded by 6 brighter ones in a triangular structure. As we will show below, this structure can be unequivocally assigned to the incorporation of a nitrogen atom in the graphene lattice in a substitutional or graphitic configuration. Therefore, the annealing process after nitrogen implantation would lead to only one kind of C–N species in this graphene/Pt(111) system.

High dependence on the bombardment energy

The bombardment energy of 100 eV used in Fig. 2b is not coincidence but a result of a study of the influence of the ion energy on the graphene/Pt(111) sample. It has been performed by means of STM measurements and LEED and AES experiments. The results of the sample preparation for three different ion energies are shown in Fig. 3.

In all the experiments, the exposure to N_2^+ source was kept for ten minutes as well as the subsequent annealing to 1000 °C. If the ion energy (E_{ions}) is set higher than 200 eV (Fig. 3a), the LEED pattern after nitrogen bombardment only displays the hexagonal structure of the (111) platinum surface. It does not show the typical ring-like structure of the graphene rotated several different degrees with respect to the metal periodicity. It suggests then a destruction of the honeycomb graphene structure due to a too intense N_2^+ bombardment. If this sample is annealed afterwards, the carbon atoms that

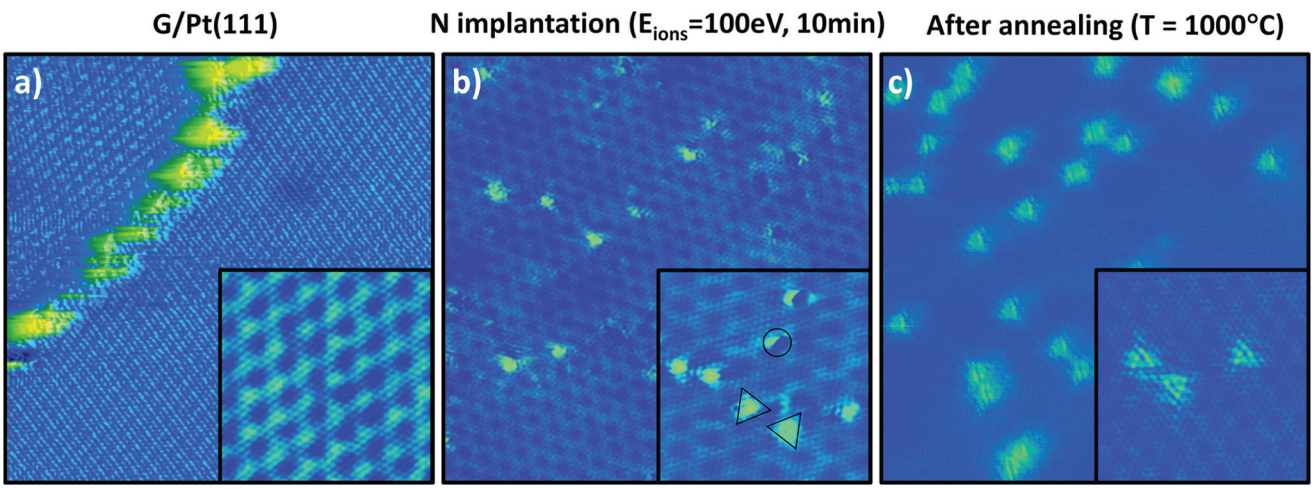

Fig. 2 STM images illustrating the sample preparation process. All figures have the same size: (20 × 20) nm^2, inset (7 × 7) nm^2; (a) pristine G/Pt(111) (V_S = −300 mV, I_T = 3.0 nA). Inset: atomic resolution image (V_S = 40 mV, I_T = 11 nA); (b) G/Pt(111) after bombardment at 100 eV during 10 min with I_{ions} = 0.02 μA (V_S = 620 mV, I_T = 0.4 nA). Inset: atomic resolution image (V_S = 400 mV, I_T = 3.8 nA); (c) G/Pt(111) after bombardment and annealing at 1000 °C (V_S = 1100 mV, I_T = 9.4 nA). Inset: atomic resolution image (V_S = 1000 mV, I_T = 4.5 nA).

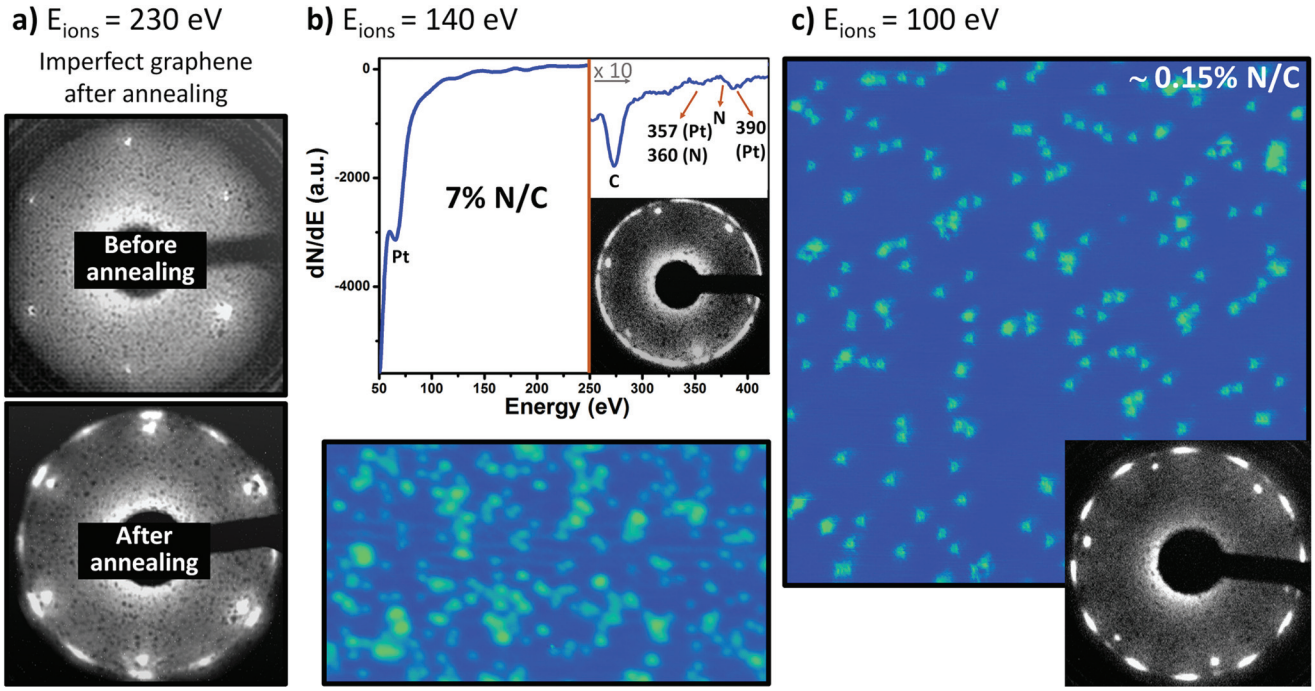

Fig. 3 LEED, STM and AES experiments that show the effect of different N bombardment energies on the preparation of N-doped G/Pt(111) surfaces. (a) E_{ions} = 230 eV (P_{N2} = 1 × 10^{-5} Torr, I_{ions} = 0.2 μA, t = 10 min). Graphene gets destroyed during bombardment. The later annealing creates defective graphene patches on the sample. This effect can be observed through the LEED pattern taken after annealing: the graphene signal is weak and diffuse (E_{LEED_before} = 61 eV, E_{LEED_after} = 64 eV). (b) E_{ions} = 140 eV (P_{N2} = 4 × 10^{-6} Torr, I_{ions} = 0.04 μA, t = 10 min). LEED pattern and AES spectra obtained using lower bombardment energy than in (a), prove the good graphene quality but that the percentage of N atoms (7% N/C) is very high. The STM measurements show that the amount of impurities in the sample is too high to tackle the structure of each one of them separately (AES primary beam energy = 2.8 keV; E_{LEED} = 62 eV; (60 × 32) nm^2 STM image: V_S = 830 mV, I_T = 1.2 nA). (c) E_{ions} = 100 eV (P_{N2} = 4 × 10^{-6} Torr, I_{ions} = 0.02 μA, t = 10 min). LEED (E_{LEED} = 63 eV) and (50 × 50) nm^2 STM image (V_S = 1100 mV, I_T = 9.4 nA) from a sample prepared with an energy of the ion gun of 100 eV. The N amount is between 0.1 and 0.2% N/C. This last preparation method is the optimum and it was selected for the rest of the analysis shown here.

remained on the surface reorganize and form defect rich and distorted graphene patches. For this reason, on the second LEED of Fig. 3a it can be observed a partial recovery of the graphene ring on the LEED measurements. By decreasing E_{ions} to ~140 eV, the graphene ring on the LEED measurements is always kept (also after ion bombardment, inset of Fig. 3b). After ion bombardment with N_2^+ and sample annealing, STM and AES experiments were performed (Fig. 3b). The STM image shows a great amount of defects on the sample but, even though all of them do look bright, it was very difficult to resolve each of them separately to analyze its structure. The differential Auger electron spectra taken on this sample confirms the presence of such quantity of nitrogen atoms on the sample: a value of 0.07 (7% N/C) is obtained from the ratio between the main peaks corresponding to the nitrogen (379 eV) and carbon (272 eV) AES transitions. Lastly, if the ion energy is decreased to ~100 eV (Fig. 3c), the graphene LEED pattern is also preserved during the whole process and the amount of nitrogen is low enough to analyze the sample properly during the STM experiments. Some statistics were done from the STM data obtaining a 0.1–0.2% N/C. This last preparation method has been used for the rest of the analysis and studies shown in this work.

Determination of the carbon–nitrogen species

All the atomic features detected in the STM images after the whole sample preparation procedure summarized in Fig. 3c are identical. As a proof of this statement an STM image is shown in the top part of Fig. 4. Identical triangular structures with atomic resolution, embedded in the moiré pattern's modulation, appear on the image.

In order to gain insight into the structural and electronic properties of the substitutional nitrogen on graphene/Pt(111), we have performed first principles calculations. First, our DFT simulations on the pristine graphene/Pt(111) surfaces show, in agreement with previous work,[39] that: (i) graphene grown on Pt(111) preserves its original flatness exhibiting a minimal geometric corrugation slightly smaller than 2 pm; (ii) the adsorption distance is 3.35 Å, larger than in many other metallic substrates and characteristic of the weakly interacting graphene–metal systems;[56] and (iii) the analysis of the electronic properties of this system points out that the Dirac cone is preserved with some distortion and a shift of ~+0.45 eV. In order to simulate substitutional nitrogen on graphene on Pt(111), as previously described in the methods section, a nitrogen atom was incorporated into graphene substituting a C atom in two

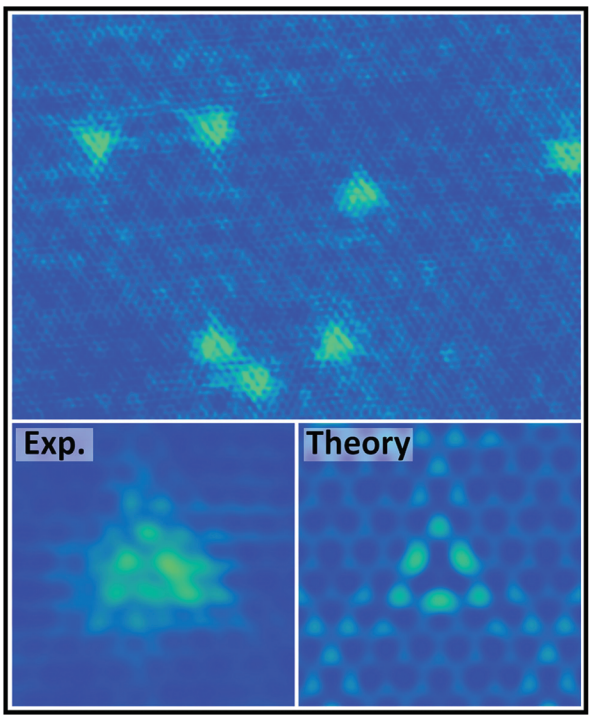

Fig. 4 Description of the structures observed by STM measurements. Top: Experimental (16 × 11.5) nm^2 STM image of N-doped graphene on Pt(111) in which nitrogen atoms are observed due to their particular triangular distribution of the density of states on their surroundings (V_S = 1100 mV, I_T = 4.5 nA). Bottom: (2 × 2) nm^2 experimental and calculated (within the Tersoff–Hamann approximation) STM images of a substitutional nitrogen on graphene/Pt(111). The moiré pattern used in the theory is the $(3 \times 3)_G$ with a 6 × 6 supercell. Experimental STM image: V_S = 1000 mV, I_T = 4.5 nA. Tersoff–Hamann image: V_S = 1000 mV, isosurface corresponding to 10^{-5} a.u.

different positions within the $(3 \times 3)_G$ moiré pattern: an atom located very close to a FCC-hollow position in the platinum surface, and in the second case, one nitrogen atom just above one platinum atom, that is, on top position. In both cases no relevant structural differences are observed. Only minimal changes in corrugation (<1 pm) and adsorption distances (<+0.5%) can be noticed. This fact could be expected as nitrogen dopants do not induce structural modifications in the G layer[33,57] unlike other elements like boron[57] or phosphorus.[58]

STM calculations following the Tersoff–Hamann approximation have been carried out to identify the structures experimentally observed. The result of this theoretical study for the substitutional nitrogen in FCC-hollow position is shown in the image labeled as "theory" in Fig. 4, in which it can be perfectly observed the good agreement between the experimental and the calculated STM images (no qualitative difference is observed in both images with the N at different positions). Notice that the nitrogen atomic concentration of the theoretical system (≈1.4% N/C) is around one order of magnitude larger than in the experiments (0.1–0.2% N/C). Still, in both, experimental and calculated images, a triangular-shape spot is observed with a dark center. The explanation of finding a dark spot despite the high PDOS on the nitrogen atoms has been deeply discussed previously in other circumstances:[21,33,59–61] the electronic states of the nitrogen on graphene are more confined in the z direction (therefore they will contribute less to the tunneling current) than those equivalent states in the surrounding carbon atoms that also have an excess of electronic charge.

Furthermore, other two nitrogen defects were simulated on the G/Pt(111) surface: pyridinic nitrogen and a nitrogen adatom. As observed in Fig. 5, their theoretical STM images are completely different from that of substitutional nitrogen. Therefore, the comparison between the experimental and the theoretical STM images leads to the confirmation that our defects in the graphene/Pt(111) surface are unequivocally identified as substitutional nitrogen atoms on the graphene lattice. Since no other kind of defects were observed on the surface, we can also conclude that nitrogen implanted following the method here described leads to the formation of only substitutional nitrogen on the graphene/Pt(111) surface.

Lastly, we show the effect of both the substrate and the nitrogen atoms on the G electronic properties as they induce opposite effects on the shift of the graphene π band: while graphitic nitrogen n-dopes the layer,[21] the Pt surface produces a p-doping effect.[62] In the case of the free standing graphene tailored with N graphitic defects, the electron distribution can be understood in terms of the localized states induced by the defect:[21,63] part of the extra electron provided by the N goes to localized states around the defect while the rest is distributed on the extended π band which is, consequently, n-doped. Our

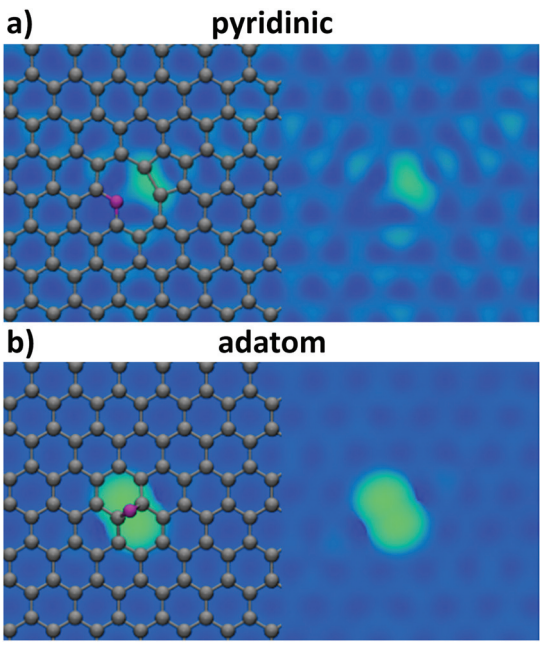

Fig. 5 (3 × 1.6) nm^2 theoretical Tersoff–Hamann images obtained at +1 V for other two kinds of simple nitrogen defects on G/Pt(111), pyridinic (a) and bridge adatom (b). In each case a ball-and-stick model is superposed with the nitrogen atom displayed in magenta. These images are calculated using iso-surface values of the local density of states corresponding to 4 × 10^{-6} a.u.

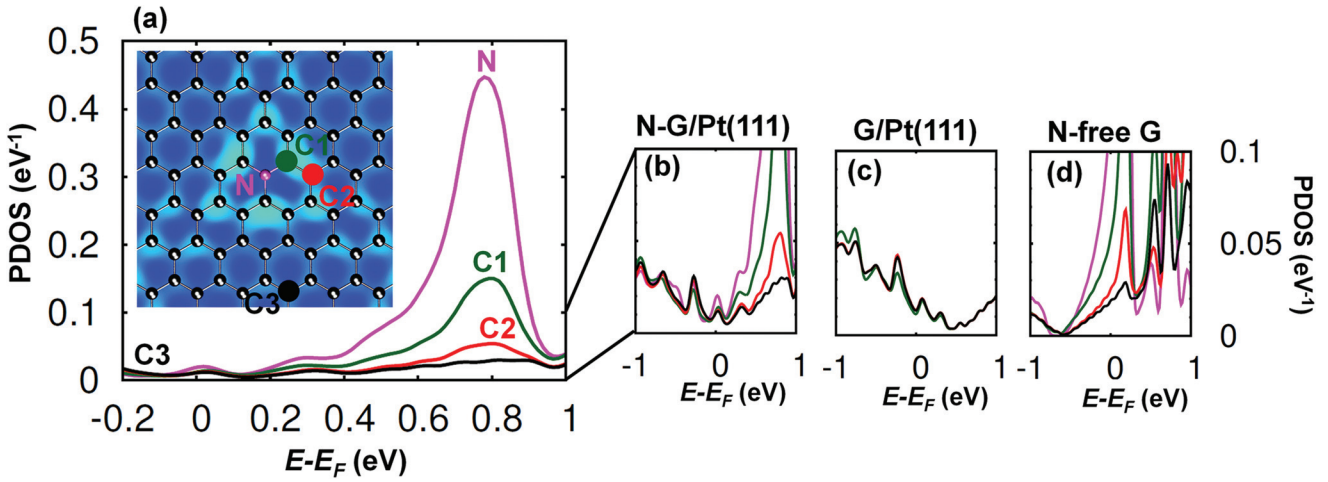

Fig. 6 Projected density of states associated with the nitrogen (pink line, N), a nearest-neighbour (green line, C1), a next-nearest-neighbour (red line, C2) and a far carbon atoms (black line, C3) for (a) the (6 × 6) G array on Pt(111) with a N-graphitic defect. The positions of the atoms have been marked on the inset showing the STM simulated image of Fig. 3. (b) A zoom of the previous PDOS. (c) PDOS of the G/Pt(111) system. And (d) PDOS of the (6 × 6) freestanding G with an N-graphitic defect.

calculated PDOS of this system (see Fig. 6d), in good agreement with previous calculations,[63] show both the nonbonding π resonances associated with the N and neighbouring C atoms in the energy range of 0.1–1 eV above the Fermi level and the shift of the graphene-π band, of about 0.5 eV, towards negative energies (for the 1.4% N/C density used in the simulations). On the other hand, the Pt surface p-dopes clean G layers. This is mainly due to the work function difference (5.7 eV and 4.2 eV for Pt(111) and G respectively) that basically induces a charge transfer from the π band of the graphene to the Pt.[62] Our calculations show that the shift of the Dirac point for a $(3 \times 3)_G$ moiré pattern is around +0.45 eV (see Fig. 6c).[39] Therefore, for the N–G/Pt(111) system a shift on the N–G states toward positive energies is expected. We show in Fig. 6a the PDOS of this system on the N and on the neighbouring C atoms as well as on a C atom far from the defect. Both the localized unbounded π states and the G-π band have been shifted around +0.6 eV due to the metal. Thus, as observed in Fig. 6a and b, in the final N–G/Pt(111) system the G-π band is not n-doped anymore but slightly empty, with a Dirac point close to +0.1 eV. Notice that the +0.6 eV shift induced by the Pt surface on the defective freestanding layer (compare Fig. 6b and d) is slightly larger than the shift on the defect free case, *i.e.* +0.45 eV (Fig. 6c). This is due to a reduction on the work function of the N tailored layer with respect to the pristine case (3.7 eV *vs.* 4.2 eV) which results in a larger charge transfer from G to the metal when the latter is incorporated. These calculations were carried out with a particular defect concentration (1.4% N/C). Any variation of this parameter, easily handled experimentally, allows the tuning of the doping of the graphene on Pt, from p-doped to n-doped at low or high defect concentrations. Although we should realize that highly defective layers would not preserve the G-π bands.

Conclusions

Using an optimized technique based on ion implantation, we have been able to grow N-doped graphene on a metallic substrate with only graphitic nitrogen incorporated on the 2D layer. Also, our theoretical analysis suggests a shift of its Dirac cone towards negative values. Our STM, LEED and AES studies of the different steps on the sample preparation have led to optimal bombardment parameters for this growth method. Our combination of experimental and theoretical STM studies have provided the ultimate test to demonstrate that the structures found on our sample can only be assigned to substitutional nitrogen on the graphene layer. Lastly, the calculated PDOS of the carbon atoms near a nitrogen atom show the doping effect of both nitrogen and the metallic Pt substrate and also explain the triangular structure found both on the simulated images and on the experimental data. As a general conclusion, our findings prove the possibility of obtaining, by this easy and effective technique, a pure substitutional nitrogen-doped graphene layer on metallic substrates with no sign of pyridinc nitrogen atoms on the lattice. The possibility of playing with the amount of dopants and, at the same time, shifting the Fermi level by changing the metal underneath, would allow the tuning of the doping on a G/metal system from p-doped to n-doped.

Acknowledgements

We thank the financial support of the Spanish MINECO (projects CSD2010-00024, MAT2011-23627, MAT2013-41636-P and MAT2014-54484-P). Computer time provided by the Spanish Supercomputer Network (RES) at the Magerit (CesViMa,

Madrid) computer. CRM is grateful to FPI-UAM graduate scholarship program and Fundación Universia for financial support. We thank Dr Lucía Rodrigo for providing preliminary results.

Notes and references

1 K. S. Novoselov, A. K. Geim, S. V. Morozov, D. Jiang, Y. Zhang, S. V. Dubonos, I. V. Grigorieva and A. A. Firsov, *Science*, 2004, **306**, 666–669.

2 J. Gonzalez, F. Guinea and M. A. H. Vozmediano, *Phys. Rev. Lett.*, 1996, **77**, 3589–3592.

3 C. Lee, X. D. Wei, J. W. Kysar and J. Hone, *Science*, 2008, **321**, 385–388.

4 A. H. Castro Neto, F. Guinea, N. M. R. Peres, K. S. Novoselov and A. K. Geim, *Rev. Mod. Phys.*, 2009, **81**, 109–162.

5 K. C. Yung, W. M. Wu, M. P. Pierpoint and F. V. Kusmartsev, *Contemp. Phys.*, 2013, **54**, 233–251.

6 A. K. Geim, *Science*, 2009, **324**, 1530–1534.

7 X. L. Li, X. R. Wang, L. Zhang, S. W. Lee and H. J. Dai, *Science*, 2008, **319**, 1229–1232.

8 X. Wang, X. Li, L. Zhang, Y. Yoon, P. K. Weber, H. Wang, J. Guo and H. Dai, *Science*, 2009, **324**, 768–771.

9 Y.-P. Lin, Y. Ksari, D. Aubel, S. Hajjar-Garreau, G. Borvon, Y. Spiegel, L. Roux, L. Simon and J.-M. Themlin, *Carbon*, 2016, **100**, 337–344.

10 P. Willke, J. A. Amani, A. Sinterhauf, S. Thakur, T. Kotzott, T. Druga, S. Weikert, K. Maiti, H. Hofsäss and M. Wenderoth, *Nano Lett.*, 2015, **15**, 5110–5115.

11 M. Telychko, P. Mutombo, P. Merino, P. Hapala, M. Ondráček, F. C. Bocquet, J. Sforzini, O. Stetsovych, M. Vondráček, P. Jelínek and M. Švec, *ACS Nano*, 2015, **9**, 9180–9187.

12 W. Zhao, O. Höfert, K. Gotterbarm, J. F. Zhu, C. Papp and H. P. Steinrück, *J. Phys. Chem. C*, 2012, **116**, 5062–5066.

13 U. Bangert, W. Pierce, D. M. Kepaptsoglou, Q. Ramasse, R. Zan, M. H. Gass, J. A. Van den Berg, C. B. Boothroyd, J. Amani and H. Hofsäss, *Nano Lett.*, 2013, **13**, 4902–4907.

14 E. H. Åhlgren, J. Kotakoski and A. V. Krasheninnikov, *Phys. Rev. B: Condens. Matter*, 2011, **83**, 115424.

15 H. Wang, T. Maiyalagan and X. Wang, *ACS Catal.*, 2012, **2**, 781–794.

16 Y. Wang, Y. Shao, D. W. Matson, J. Li and Y. Lin, *ACS Nano*, 2010, **4**, 1790–1798.

17 Z.-H. Sheng, L. Shao, J.-J. Chen, W.-J. Bao, F.-B. Wang and X.-H. Xia, *ACS Nano*, 2011, **5**, 4350–4358.

18 D. Geng, Y. Chen, Y. Chen, Y. Li, R. Li, X. Sun, S. Ye and S. Knights, *Energy Environ. Sci.*, 2011, **4**, 760–764.

19 L. Qu, Y. Liu, J.-B. Baek and L. Dai, *ACS Nano*, 2010, **4**, 1321–1326.

20 D. C. Wei, Y. Q. Liu, Y. Wang, H. L. Zhang, L. P. Huang and G. Yu, *Nano Lett.*, 2009, **9**, 1752–1758.

21 L. Zhao, R. He, K. T. Rim, T. Schiros, K. S. Kim, H. Zhou, C. Gutiérrez, S. P. Chockalingam, C. J. Arguello, L. Pálová, D. Nordlund, M. S. Hybertsen, D. R. Reichman, T. F. Heinz, P. Kim, A. Pinczuk, G. W. Flynn and A. N. Pasupathy, *Science*, 2011, **333**, 999–1003.

22 D. Usachov, A. Fedorov, O. Vilkov, B. Senkovskiy, V. K. Adamchuk, L. V. Yashina, A. A. Volykhov, M. Farjam, N. I. Verbitskiy, A. Grüneis, C. Laubschat and D. V. Vyalikh, *Nano Lett.*, 2014, **14**, 4982–4988.

23 R. J. Koch, M. Weser, W. Zhao, F. Viñes, K. Gotterbarm, S. M. Kozlov, O. Höfert, M. Ostler, C. Papp, J. Gebhardt, H. P. Steinrück, A. Görling and T. Seyller, *Phys. Rev. B: Condens. Matter*, 2012, **86**, 075401.

24 D. Usachov, O. Vilkov, A. Grüneis, D. Haberer, A. Fedorov, V. K. Adamchuk, A. B. Preobrajenski, P. Dudin, A. Barinov, M. Oehzelt, C. Laubschat and D. V. Vyalikh, *Nano Lett.*, 2011, **11**, 5401–5407.

25 A. L. Pinardi, G. Otero-Irurueta, I. Palacio, J. I. Martinez, C. Sanchez-Sanchez, M. Tello, C. Rogero, A. Cossaro, A. Preobrajenski, B. Gómez-Lor, A. Jancarik, I. G. Stará, I. Starý, M. F. Lopez, J. Méndez and J. A. Martin-Gago, *ACS Nano*, 2013, **7**, 3676–3684.

26 V. D. Pham, J. Lagoute, O. Mouhoub, F. Joucken, V. Repain, C. Chacon, A. Bellec, Y. Girard and S. Rousset, *ACS Nano*, 2014, **8**, 9403–9409.

27 Y. Tison, J. Lagoute, V. Repain, C. Chacon, Y. Girard, S. Rousset, F. Joucken, D. Sharma, L. Henrard, H. Amara, A. Ghedjatti and F. Ducastelle, *ACS Nano*, 2015, **9**, 670–678.

28 F. Joucken, Y. Tison, J. Lagoute, J. Dumont, D. Cabosart, B. Zheng, V. Repain, C. Chacon, Y. Girard, A. R. Botello-Méndez, S. Rousset, R. Sporken, J.-C. Charlier and L. Henrard, *Phys. Rev. B: Condens. Matter*, 2012, **85**, 161408.

29 J. Lagoute, F. Joucken, V. Repain, Y. Tison, C. Chacon, A. Bellec, Y. Girard, R. Sporken, E. H. Conrad, F. Ducastelle, M. Palsgaard, N. P. Andersen, M. Brandbyge and S. Rousset, *Phys. Rev. B: Condens. Matter*, 2015, **91**, 125442.

30 K. J. Kim, H. Lee, J. Choi, H. Lee, M. C. Jung, H. J. Shin, T. H. Kang, B. Kim and S. Kim, *J. Phys.: Condens. Matter*, 2010, **22**, 045005.

31 P. Willke, J. A. Amani, S. Thakur, S. Weikert, T. Druga, K. Maiti, H. Hofsäss and M. Wenderoth, *Appl. Phys. Lett.*, 2014, **105**, 111605.

32 F. Xu, M. Minniti, P. Barone, A. Sindona, A. Bonanno and A. Oliva, *Carbon*, 2008, **46**, 1489–1496.

33 M. Telychko, P. Mutombo, M. Ondráček, P. Hapala, F. C. Bocquet, J. Kolorenč, M. Vondráček, P. Jelínek and M. Švec, *ACS Nano*, 2014, **8**, 7318–7324.

34 Z. Hou and K. Terakura, *J. Phys. Chem. C*, 2015, **119**, 4922–4933.

35 J. Kotakoski, A. V. Krasheninnikov, Y. Ma, A. S. Foster, K. Nordlund and R. M. Nieminen, *Phys. Rev. B: Condens. Matter*, 2005, **71**, 205408.

36 J. Wintterlin and M. L. Bocquet, *Surf. Sci.*, 2009, **603**, 1841–1852.

37 C. Johann, T. N. D. Alpha, E. Martin, B. Carsten, W. Dirk, B. Niemma, J. M. Z. H. Frank, G. Raoul van, P. Bene and M. Thomas, *New J. Phys.*, 2009, **11**, 023006.

38 P. Sutter, J. T. Sadowski and E. Sutter, *Phys. Rev. B: Condens. Matter*, 2009, **80**, 245411.
39 M. M. Ugeda, D. Fernandez-Torre, I. Brihuega, P. Pou, A. J. Martinez-Galera, R. Perez and J. M. Gomez-Rodriguez, *Phys. Rev. Lett.*, 2011, **107**, 116803.
40 O. Custance, S. Brochard, I. Brihuega, E. Artacho, J. M. Soler, A. M. Baro and J. M. Gomez-Rodriguez, *Phys. Rev. B: Condens. Matter*, 2003, **67**, 235410.
41 A. J. Martinez-Galera and J. M. Gomez-Rodriguez, *J. Phys. Chem. C*, 2011, **115**, 11089–11094.
42 A. T. N'Diaye, R. van Gastel, A. J. Martinez-Galera, J. Coraux, H. Hattab, D. Wall, F. J. M. zu Heringdorf, M. Horn-von Hoegen, J. M. Gomez-Rodriguez, B. Poelsema, C. Busse and T. Michely, *New J. Phys.*, 2009, **11**, 113056.
43 I. Horcas, R. Fernandez, J. M. Gomez-Rodriguez, J. Colchero, J. Gomez-Herrero and A. M. Baro, *Rev. Sci. Instrum.*, 2007, **78**, 013705.
44 G. Kresse and J. Furthmüller, *Phys. Rev. B: Condens. Matter*, 1996, **54**, 11169–11186.
45 P. E. Blöchl, *Phys. Rev. B: Condens. Matter*, 1994, **50**, 17953–17979.
46 G. Kresse and D. Joubert, *Phys. Rev. B: Condens. Matter*, 1999, **59**, 1758–1775.
47 J. P. Perdew, K. Burke and M. Ernzerhof, *Phys. Rev. Lett.*, 1996, **77**, 3865–3868.
48 S. Grimme, *J. Comput. Chem.*, 2006, **27**, 1787–1799.
49 B. de la Torre, M. Ellner, P. Pou, N. Nicoara, R. Perez and J. M. Gomez-Rodriguez, *Phys. Rev. Lett.*, 2016, **116**, 245502.
50 P. Merino, M. Švec, A. L. Pinardi, G. Otero and J. A. Martín-Gago, *ACS Nano*, 2011, **5**, 5627–5634.
51 J. Tersoff and D. R. Hamann, *Phys. Rev. Lett.*, 1983, **50**, 1998–2001.
52 A. J. Martinez-Galera and J. M. Gomez-Rodriguez, *J. Phys. Chem. C*, 2011, **115**, 23036–23042.
53 L. Köhler, S. Scaglione, R. Giorgi, J. Riga, P. Rudolf and R. Caudano, *Surf. Interface Anal.*, 2000, **29**, 647–652.
54 D. Van Vechten, G. K. Hubler and E. P. Donovan, *Vacuum*, 1986, **36**, 841–845.
55 P. Hammer and W. Gissler, *Diamond Relat. Mater.*, 1996, **5**, 1152–1158.
56 M. Batzill, *Surf. Sci. Rep.*, 2012, **67**, 83–115.
57 L. Ferrighi, M. I. Trioni and C. Di Valentin, *J. Phys. Chem. C*, 2015, **119**, 6056–6064.
58 E. Cruz-Silva, F. Lopez-Urias, E. Munoz-Sandoval, B. G. Sumpter, H. Terrones, J. C. Charlier, V. Meunier and M. Terrones, *ACS Nano*, 2009, **3**, 1913–1921.
59 B. Zheng, P. Hermet and L. Henrard, *ACS Nano*, 2010, **4**, 4165–4173.
60 S.-O. Guillaume, B. Zheng, J.-C. Charlier and L. Henrard, *Phys. Rev. B: Condens. Matter*, 2012, **85**, 035444.
61 P. Lambin, H. Amara, F. Ducastelle and L. Henrard, *Phys. Rev. B: Condens. Matter*, 2012, **86**, 045448.
62 G. Giovannetti, P. A. Khomyakov, G. Brocks, V. M. Karpan, J. van den Brink and P. J. Kelly, *Phys. Rev. Lett.*, 2008, **101**, 026830.
63 T. Schiros, D. Nordlund, L. Palova, D. Prezzi, L. Y. Zhao, K. S. Kim, U. Wurstbauer, C. Gutierrez, D. Delongchamp, C. Jaye, D. Fischer, H. Ogasawara, L. G. M. Pettersson, D. R. Reichman, P. Kim, M. S. Hybertsen and A. N. Pasupathy, *Nano Lett.*, 2012, **12**, 4025–4031.